AIP | Review of Scientific Instruments

Proton pinhole imaging on the National Ignition Facility

A. B. Zylstra, H.-S. Park, J. S. Ross, F. Fiuza, J. A. Frenje, D. P. Higginson, C. Huntington, C. K. Li, R. D. Petrasso, B. Pollock, B. Remington, H. G. Rinderknecht, D. Ryutov, F. H. Séguin, D. Turnbull, and S. C. Wilks

Citation: Review of Scientific Instruments **87**, 11E704 (2016); doi: 10.1063/1.4959782
View online: http://dx.doi.org/10.1063/1.4959782
View Table of Contents: http://scitation.aip.org/content/aip/journal/rsi/87/11?ver=pdfcov
Published by the AIP Publishing

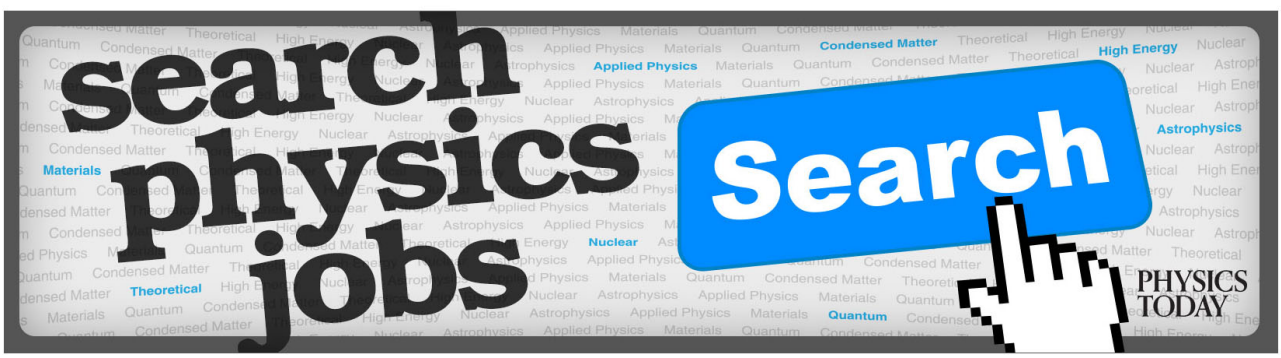

Proton pinhole imaging on the National Ignition Facility

A. B. Zylstra,[1,a)] H.-S. Park,[2] J. S. Ross,[2] F. Fiuza,[3] J. A. Frenje,[4] D. P. Higginson,[2] C. Huntington,[2] C. K. Li,[4] R. D. Petrasso,[4] B. Pollock,[2] B. Remington,[2] H. G. Rinderknecht,[2] D. Ryutov,[2] F. H. Séguin,[4] D. Turnbull,[2] and S. C. Wilks[2]
[1]*Los Alamos National Laboratory, Los Alamos, New Mexico 87545, USA*
[2]*Lawrence Livermore National Laboratory, Livermore, California 94550, USA*
[3]*SLAC National Accelerator Laboratory, Menlo Park, California 94025, USA*
[4]*Plasma Science and Fusion Center, Massachusetts Institute of Technology, Cambridge, Massachusetts 02139, USA*

(Presented 9 June 2016; received 5 June 2016; accepted 27 June 2016; published online 29 July 2016)

Pinhole imaging of large (mm scale) carbon-deuterium (CD) plasmas by proton self-emission has been used for the first time to study the microphysics of shock formation, which is of astrophysical relevance. The 3 MeV deuterium-deuterium (DD) fusion proton self-emission from these plasmas is imaged using a novel pinhole imaging system, with up to five different 1 mm diameter pinholes positioned 25 cm from target-chamber center. CR39 is used as the detector medium, positioned at 100 cm distance from the pinhole for a magnification of 4×. A Wiener deconvolution algorithm is numerically demonstrated and used to interpret the images. When the spatial morphology is known, this algorithm accurately reproduces the size of features larger than about half the pinhole diameter. For these astrophysical plasma experiments on the National Ignition Facility, this provides a strong constraint on simulation modeling of the experiment. *Published by AIP Publishing.* [http://dx.doi.org/10.1063/1.4959782]

I. INTRODUCTION

Determining the shape, spatial scale, and location of particle emission is an important diagnostic of hot high-energy-density plasmas on the National Ignition Facility (NIF),[1] such as those produced in laboratory astrophysics and inertial-confinement fusion (ICF) experiments. Fusion self-emission imaging is a measure of the local thermonuclear reaction rate. Until now, imaging the self-emission of fusion plasmas was limited to x-ray pinhole[2] and penumbral[3] imaging, neutron pinhole[4] and penumbral[5] imaging, or penumbral imaging of protons.[6–8] When studying implosions, penumbral imaging must be used for protons due to the combination of low yields and small spatial scales. For a typical[7] proton yield of $\sim 10^{10}$ from an imploded core 50–80 μm in diameter, a 10 μm diameter pinhole 10 cm from the implosion would allow only 6 protons to reach the detector.

Recent experiments on shock formation[9–12] relevant to astrophysics study hot mm-scale carbon-deuterium (CD) plasmas, which generate the reactions

$$\mathrm{D} + \mathrm{D} \rightarrow \mathrm{p}\ (3.02\ \mathrm{MeV}) + \mathrm{T}\ (1.01\ \mathrm{MeV}) \quad (1)$$

$$\rightarrow \mathrm{n}\ (2.45\ \mathrm{MeV}) + {}^{3}\mathrm{He}\ (0.82\ \mathrm{MeV}). \quad (2)$$

The 3 MeV proton from Eq. (1) is used in this work. The two reaction branches have comparable cross sections.[13] The neutron yield[14] and production time[15] are measured, but the spatial distribution of neutron emission cannot be measured. However, with proton yields of 10^8–10^{10} produced over a region several mm in scale, the proton self-emission from these plasmas can be imaged using a pinhole camera. We report the first proton pinhole imaging instrument for high-energy-density plasmas, which is organized as follows: the instrument design is described in Section II, the data and analysis are discussed in Section III, and the paper is concluded in Section IV.

II. INSTRUMENT DESIGN

The design of this instrument is shown in Fig. 1. The source of protons (left) is imaged using a pinhole and detector pack (right). The source-pinhole distance is 25 cm and the pinhole-detector distance is 100 cm for a magnification of 4×. The detector pack consists of a front filter (12.5 μm of Ta to range out laser-accelerated ions,[16] which are several orders of magnitude more numerous than fusion products), a piece of CR-39 to detect the protons,[17] and an image plate for co-registered x-ray imaging using the same pinhole. Up to five pinholes can be used in an array (bottom left). The slits adjacent to the pinholes are used for simultaneous x-ray spectroscopy using the NIF "Supersnout II" crystal spectrometer.[18] Using this configuration, proton pinhole imaging can be accomplished using approximately mm diameter pinholes, because of the large plasmas in these experiments, with adequate proton statistics (10^2–10^4) for the above yield range.

The CR-39 data are processed using standard techniques[17] to record the proton track distribution. The CR-39 is etched in 6N NaOH for 2–5 h, depending on proton fluence,

Note: Contributed paper, published as part of the Proceedings of the 21st Topical Conference on High-Temperature Plasma Diagnostics, Madison, Wisconsin, USA, June 2016.

a)Electronic mail: zylstra@lanl.gov

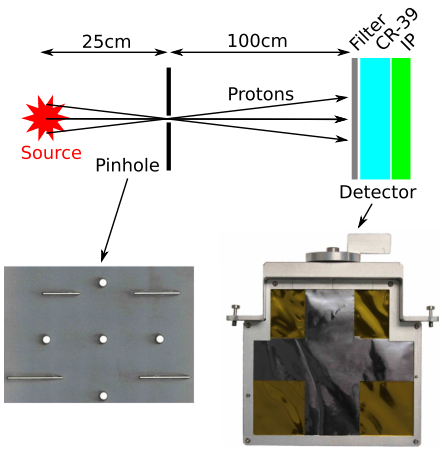

FIG. 1. Proton pinhole imaging instrument. Top: schematic showing the source, pinhole, and detector pack. Bottom right: image of the detector pack, bottom left: image of 5 pinhole array.

and then scanned using a digital microscope system that records characteristics of each track. Background is rejected using specified ranges in the track diameter, contrast, and eccentricity. In these experiments, the primary source of background is the intrinsic noise in the CR39, with typical S/B of 10–100×. The remaining signal tracks are spatially histogrammed to create an image.

III. DATA AND DECONVOLUTION ANALYSIS

Raw data from NIF shot N150616-001-999 are shown in Fig. 2. In the raw data, there are five independent images (see Fig. 1), each from a different 1 mm diameter pinhole. The color scale corresponds to protons per pixel. The proton yield on this shot was 2×10^9, about an average for this type of experiment. The spatial scale is given at the detector plane. Since the magnification is 4×, it is clear that the object size is several mm, which means that the pinhole point-spread function (PSF) is non-negligible.

To remove the effect of the finite pinhole size, we perform a 2-D image reconstruction using a Wiener deconvolution.[19,20]

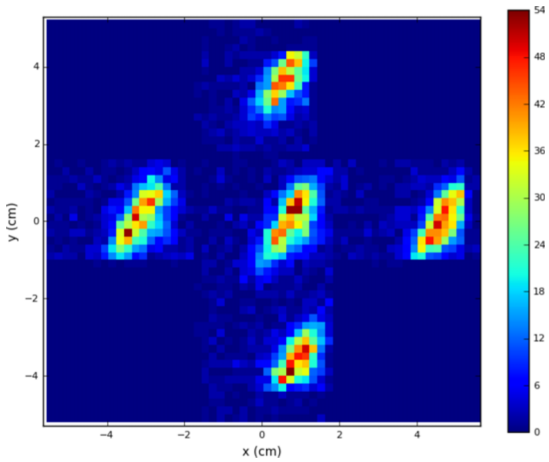

FIG. 2. Raw data from shot N150616-001-999, showing five pinhole images. All pinholes were 1 mm diameter. Data are shown in protons per pixel. The spatial scale is at the detector plane.

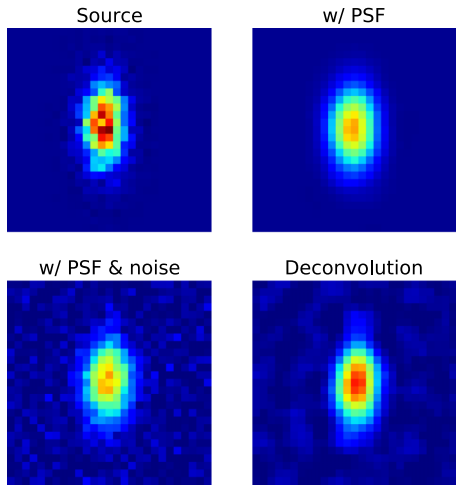

FIG. 3. Deconvolution algorithm demonstration. A synthetic source (top left) with statistical noise is convolved with a 1 mm pinhole PSF (top right) and representative detector noise (bottom left), which is then deconvolved (bottom right) reconstructing the original image. The synthetic source has comparable proton yield to the real data shown in Fig. 2. Each plot is 4×4 mm at the image plane.

Because of the relatively low particle statistics, the Wiener deconvolution minimizes the effect of noise on the inferred results. The fidelity of this algorithm is demonstrated in Fig. 3 using synthetic data. A 2-D Gaussian source profile is used with $\sigma_x = 0.5$ mm and $\sigma_y = 1.0$ mm, shown in the upper left. The synthetic source includes statistical noise consistent with a 2×10^9 proton yield, as in shot N150616-001-999. This source profile is convolved with the pinhole PSF (top right) and then detector noise is added (bottom left) to generate the synthetic data. The deconvolution algorithm accurately reconstructs the source under these conditions (bottom right). A fit to the reconstructed image gives $\sigma_x = 0.51$ mm and $\sigma_y = 1.0$ mm, demonstrating that the spatial extent is accurately deconvolved.

To test the limits of this technique, the synthetic data reconstruction routine, as in Fig. 3, was run for varying values of the "thin" width, σ_x, and pinhole diameter. 50 randomized reconstructions were performed for each point in Fig. 4, which

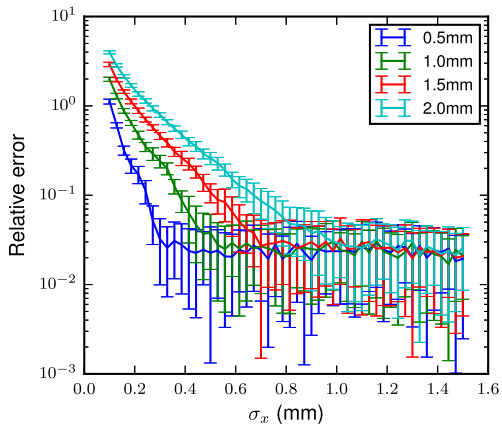

FIG. 4. Deconvolution algorithm relative error in reconstructing σ_x, the small dimension, versus σ_x for various pinhole diameters (0.5, 1.0, 1.5, and 2.0 mm). The error bars are the standard deviation in 50 simulation runs at each point.

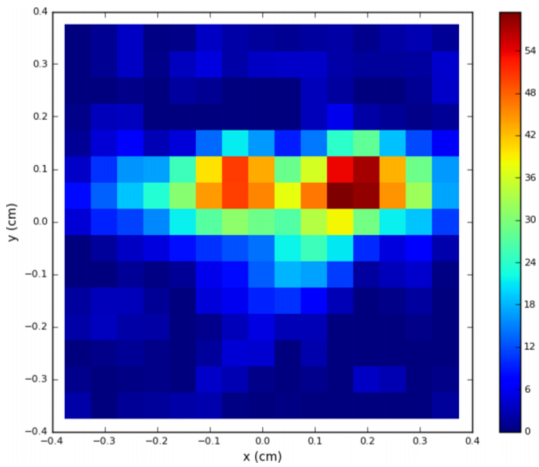

FIG. 5. Deconvolved data from Fig. 2 (shot N150616-001-999), central pinhole. The color scale corresponds to protons per pixel. The image has been rotated, so the long axis of the source is horizontal. Spatial dimensions are at the source plane.

shows pinhole diameters of d_{ph} = 0.5, 1.0, 1.5, and 2.0 mm. The relative error in σ_x from a fit to the reconstruction is shown, where the relative error is $|\sigma_{x,fit} - \sigma_x|/\sigma_x$. For image features much smaller than the pinhole size, the reconstruction is unreliable. However, for image features $\gtrsim d_{ph}/2$ the size is accurately reconstructed, if the source morphology is known.

The Wiener deconvolution routine is applied to the data from shot N150616-001-999 and shown in Fig. 5. The deconvolved image is rotated, and shown with spatial dimensions corresponding to the source size. The hot proton emitting region in this shot is clearly elongated along one axis. Two statistically significant bright features are observed within the hot region.

This diagnostic enables new and unique constraints of simulations of these experiments. Simulations are performed using radiation-hydrodynamics and particle-in-cell techniques. All of these simulations give the plasma conditions over the experiment, which can be used to create synthetic proton self-emission data by the local fusion reactivity. This imaging technique therefore significantly constrains the models, in particular their ability to predict the proton yield and geometry of the emitting region.

IV. CONCLUSIONS

The first proton pinhole imaging diagnostic for high-energy-density plasmas has been implemented on the NIF. Recent experiments have been conducted that produce large (mm-scale) CD plasmas to study the microphysics of shock formation, which is relevant to shocks in astrophysical systems. The hot and dense regions of these plasmas produce 3 MeV DD protons, which are imaged using a new pinhole detector. The pinhole images are reconstructed using a Wiener deconvolution algorithm, which is numerically demonstrated for synthetic data. This diagnostic will provide strong constraints on modeling of these astrophysically relevant plasmas.

Depending on the system to be imaged, this technique can be extended in several ways. Other charged fusion products, for example, D^3He protons (14.7 MeV) or DT αs (3.5 MeV), could be imaged by changing the detector pack filter (Fig. 1). The imaging resolution or field of view can also be changed with different magnifications—1× and 12× are available with existing NIF hardware.

ACKNOWLEDGMENTS

We thank the operations and engineering staff at NIF for supporting these experiments, and M. Valadez for her work processing the CR-39. This work was supported in part by the U.S. DoE (Grant Nos. DE-NA0001857, DE-FC52-08NA28752, DE-FG02-88ER40387, DE-NA0001837, and DE-AC52-06NA25396), by NSF (Grant No. 1122374), and by the U.S. DoE Office of Fusion Energy Sciences. This work performed under the auspices of the U.S. DoE by LANL under Contract No. DE-AC62-06NA25396 and by LLNL under Contract No. DE-AC52-07NA27344 and supported by the Laboratory Directed Research and Development Program at LANL (Grant No. 20150717PRD2) and at LLNL (Grant No. 15-ERD-065).

[1]G. H. Miller, E. I. Moses, and C. R. Wuest, Nucl. Fusion **44**, S228 (2004).
[2]T. Ma *et al.*, Rev. Sci. Instrum. **83**, 10E115 (2012).
[3]B. Bachmann *et al.*, Rev. Sci. Instrum. **85**, 11D614 (2014).
[4]F. E. Merrill *et al.*, Rev. Sci. Instrum. **83**, 10D317 (2012).
[5]L. Disdier *et al.*, Phys. Plasmas **13**, 056317 (2006).
[6]F. H. Séguin *et al.*, Rev. Sci. Instrum. **75**, 3520–3525 (2004).
[7]J. R. Rygg *et al.*, Rev. Sci. Instrum. **86**, 116104 (2015).
[8]F. H. Séguin *et al.*, Phys. Plasmas **23**, 032705 (2016).
[9]C. M. Huntington *et al.*, Nat. Phys. **11**, 173–178 (2015).
[10]H. S. Park *et al.*, Phys. Plasmas **22**, 056311 (2015).
[11]H. S. Park *et al.*, J. Phys.: Conf. Ser. **688**, 012084 (2016).
[12]J. S. Ross *et al.*, "Transition from collisional to collisionless regimes in interpenetrating plasma flows on the National Ignition Facility" (unpublished).
[13]R. E. Brown and N. Jarmie, Phys. Rev. C **41**, 1391–1400 (1990).
[14]V. Y. Glebov *et al.*, Rev. Sci. Instrum. **77**, 10E715 (2006).
[15]H. Rinderknecht *et al.*, Rev. Sci. Instrum. **83**, 10D902 (2012).
[16]D. G. Hicks *et al.*, Phys. Plasmas **8**, 606 (2001).
[17]F. H. Séguin *et al.*, Rev. Sci. Instrum. **74**, 975–995 (2003).
[18]S. Regan, private communication (2013).
[19]Scikit-image: Image processing in python, 2015, http://scikit-image.org/.
[20]F. Oreux, J.-F. Giovannelli, and T. Rodet, J. Opt. Soc. Am. A **27**, 1593–1607 (2010).